High-Temperature Hydrogen Attack on 2.25Cr-1Mo Steel: The Roles of Residual Carbon, Initial Microstructure and Carbide Stability

ORIGINAL RESEARCH ARTICLE

High-Temperature Hydrogen Attack on 2.25Cr-1Mo Steel: The Roles of Residual Carbon, Initial Microstructure and Carbide Stability

M.A.M. ALSHAHRANI, S.W. OOI, M. HÖRNQVIST COLLIANDER, G.M.A.M. EL-FALLAH, and H.K.D.H. BHADESHIA

High temperature hydrogen attack is a damage mechanism that occurs in critical steel components in petrochemical plants and refineries when the hydrogen penetrates the steel and reacts with the carbides within to produce pores containing methane. With the motivation of understanding the role of carbide stability on the reaction with hydrogen, samples of a classic $2\frac{1}{4}$Cr-1Mo steel were subjected to a variety of heat treatments that generate a corresponding variety of precipitates, prior to exposure to high-pressure hydrogen in an autoclave. Using quantitative carbide, porosity and microstructural characterisation, it has been possible to demonstrate the roles of four variables: (a) the carbon residue present in the ferrite; (b) the non-equilibrium chemical composition of carbide; (c) the fraction of the carbide that is closest to the thermodynamic equilibrium state and (d) the initial microstructural state, i.e., whether it is martensitic or bainitic prior to heat treatment.

https://doi.org/10.1007/s11661-022-06809-9

I. INTRODUCTION

HYDROGEN embrilttlement is one of the mechanisms that threatens the integrity of steel equipment in the oil and gas industry. The atomic hydrogen is the cause of the embrittlement.[1] The dissociation of molecular hydrogen into nascent atomic hydrogen at the steel surface commonly occurs by the chemical reaction caused by corrosion or cathodic protection at the steel surface. The nascent hydrogen atoms fail to recombine at the surface due to the presence of poisoners such as hydrogen sulfide and cyanides. The atomic hydrogen then diffuses into the steel.[2,3] However, in the absence of an aqueous environment, i.e., high-temperature environments, the corrosion reaction is eliminated at the surface. Molecular hydrogen then dissociates under the high pressure of the environment at the steel surface, which is the hydrogen dissociation mechanism in high-temperature, high-pressure hydrogen attack that is discussed in this paper.

Apart from accumulating at stress-fields such as inclusions and ferrite/carbide interfaces, the diffusable atomic hydrogen reacts chemically with the carbon that is tied up in carbides to form methane bubbles which become a permanent feature of the steel as they are too large to diffuse out, as seen in the following reaction: $C + 2H_2 \leftrightarrow CH_4$. The methane reaction occurs preferentially at the least stable carbide, cementite, as follows: $Fe_3C + 2H_2 \leftrightarrow CH_4 + 3Fe$. The reaction can still take place to a lesser extent at other substitutionally alloyed carbides that are precipitated in creep-resisting steels, for example, M_2C, M_7C_3, $M_{23}C_6$ etc., where 'M' stands for a mixture of metal atoms. The formation of methane-containing bubbles leads to internal stresses that weaken grain boundaries, which eventually lead to the formation of microcracks and ultimate failure under the influence of the external stresses that the component is designed to support or even by the local creep introduced by the bubble formation.[4–16] It could be argued, therefore, carbides that are more thermodynamically stable in steel should result in an enhanced resistance to hydrogen attack.[17,18] The problem is

M.A.M. ALSHAHRANI is with the Materials Science and Metallurgy, University of Cambridge, Cambridge CB2 3QZ, UK and also with the Saudi Aramco Research and Development Centre, Dhahran 34466, Saudi Arabia. Contact e-mail: mohammed.shahrani.34@aramco.com S.W. OOI is with the Materials Science and Metallurgy, University of Cambridge. M. HÖORNQVIST COLLIANDER is with the Department of Physics, Chalmers University of Technology, Göteborg 41296, Sweden. G.M.A.M. EL-FALLAH is with the School of Engineering, University of Leicester, Leicester LE1 7RH, UK. H.K.D.H. BHADESHIA is with the Materials Science and Metallurgy, University of Cambridge and also with the School of Engineering and Materials Science, Queen Mary University of London, London E1 4NS, UK.
Manuscript submitted May 13, 2022; accepted August 21, 2022.

Published online: 08 October 2022

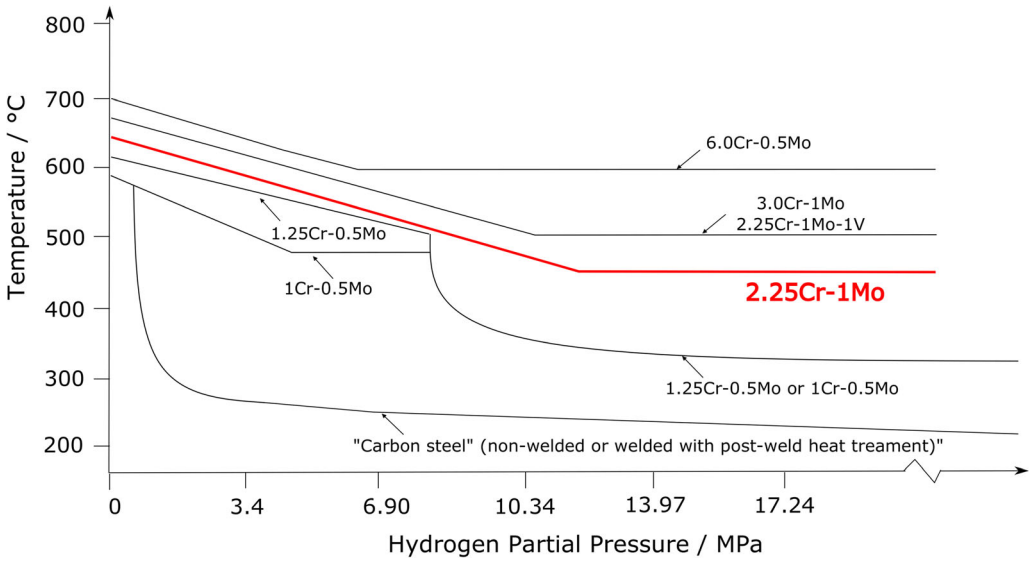

Fig. 1—The *Nelson curves* used for designing against hydrogen attack. The area below each curve represents the safe operating zone for the corresponding steel. In red is the 2.25Cr-1Mo steel studied in this work. Adapted from Ref. [22] (Color figure online).

important because failures of the steel in petrochemical plant can on rare occasions lead to fatal catastrophes such as at the Tesoro Anacortes Refinery;[19] more commonly, the attack requires the costly replacement of components.[20]

The current best practice for design against hydrogen attack uses an experience-based approach, expressed as the *Nelson curves*,[21] Figure 1.[22] These curves define the temperature and hydrogen pressure at which established steels can operate without the risk of hydrogen attack. The curves suggest that carbides-based Cr, Mo and V are less likely to be reduced by hydrogen.[23,24] However, although the average composition is clearly an important factor, it is possible in each of these steels to generate a variety of microstructures so the Nelson curves do not represent the full picture. Heat treatments could play a major role in precipitating specific carbides that resist hydrogen attack. There is a general feeling that design based on a better understanding of the mechanism and kinetics of attack may lead to better utilisation of existing steels or the development of new ones that better resist the attack.[14,25]

Studies on a commercially used $2\frac{1}{4}$Cr-1Mo steel have shown that the equilibrium carbide, $M_{23}C_6$ ('M' stands for metal atoms) is resistant to hydrogen attack when compared with cementite; however, there are discrepancies in the perceived order of stability in mixtures of M_7C_3, M_2C and M_6C.[4,26]

The present work assesses the $2\frac{1}{4}$Cr-1Mo steel in a variety of microstructural states in order to explicitly reveal the hydrogen-reaction resistance of precipitated carbides. Quantitative methods based on synchrotron X-ray diffraction and microscopy have been used to characterise samples exposed to high temperature, high-pressure hydrogen. It will be shown that the experimental data can be consistently interpreted within a thermodynamic framework of phase stabilities.

II. EXPERIMENTAL PROCEDURE

A. *Material and Heat Treatment*

The steel was supplied by British Petroleum. It was electroslag-remelted and then forged to produce a homogeneous component. There was, therefore, nothing in the metallography of the samples that indicated chemical segregation. All the samples were cut from adjacent positions so we do not expect variations in inclusion density between the samples.

Carbon is usually present within the steel in the form of carbides. The work here is focused on relating the depletion of carbides due to hydrogen attack on $2\frac{1}{4}$Cr-1Mo steel to the heat treatment, tempering conditions and deviation from equilibrium. The composition of the actual steel used is listed in Table I.

The heat treatments were selected based on the work of Baker and Nutting.[27,28] A number of combinations of carbides could be generated to reveal their influence on hydrogen attack resistance. Five specimens, cubes with a side length of ≈ 2.5 cm, were austenitised for 2 h at 960 °C. Two of the cubes were then quenched into water with the remainder air cooled. Each cube then was subjected to a different heat-treatment in order to induce a variety of carbide mixtures; we note that the carbide compositions in terms of the metal atoms are also sensitive to the heat-treatment temperature. The details are listed in Table II.

B. *Hydrogen Exposure*

Judging from Figure 1, the $2\frac{1}{4}$Cr-1Mo steel is expected to be susceptible to attack if the temperature exceeds 450°C when the hydrogen partial pressure exceeds 13.7 MPa. The equipment used was at The Welding Institute (TWI), which can achieve up to 525 °C and a hydrogen pressure of 10 MPa, the precise conditions used in the present work. The TWI autoclave was used

Table I. Chemical Composition (Weight Pct) of the $2\frac{1}{4}$Cr-1Mo Used

C	Si	Cr	Mo	Ni	Mn	P	S	Cu	Al	V
0.14	0.1	2.24	0.97	0.37	0.42	0.007	0.001	0.04	0.043	0.005

Table II. Heat Treatments Performed on Different $2\frac{1}{4}$Cr-1Mo Specimens

Sample	Heat Treatment	Carbides Expected[28]
A	Quench, temper @ 650°C, 50 h	$M_6C + M_2C + M_7C_3$
B	Quench, temper @ 700°C, 1 h	$M_3C + M_2C + M_7C_3$
C	Air-cool, temper @ 650°C, 50 h	$M_6C + M_2C + M_7C_3$
D	Air-cool, temper @ 700°C, 50 h	$M_{23}C_6 + M_6C + M_2C + M_7C_3$
E	Air-cool, temper @ 750°C, 5 h	$M_{23}C_6 + M_6C + M_2C + M_7C_3$

at maximum capacity for 20 days to be consistent with the work of Wanagel *et al.*,[29] although the parameters possible on the TWI autoclave are less severe that those in Reference 29. It also is costly to use the facility so longer exposures could not be accommodated. The specimens were polished before hydrogen exposure with no visible signs of oxide, and then placed into the hydrogen chamber. There were no differences found in the surfaces after exposure, between the different heat treatments.

C. *Characterisation*

The characterisation focused on the comparison of results before and after hydrogen exposure to give a clear picture of damage evolution:

- as the carbide reacts with hydrogen, it leaves behind a methane-filled void which can be imaged and measured using microscopy on unetched specimens. The images were then processed using *ImageJ* software to determine the area fraction occupied by voids.
  The FEI Tecnai Osiris FEG TEM, fitted with an energy dispersive spectroscopy detector, was used for microstructural characterisation of fine carbides, as well as carbide identification. The microscope has an accelerating voltage of 200 kV. Carbide reflections were identified using diffraction patterns, while their morphology and orientation were revealed with dark-field imaging. Scanning transmission microscopy was used for high resolution imaging of fine carbides.
- Synchrotron X-ray analysis was used to measure how the carbide volume fractions have changed following hydrogen exposure. The diffraction intensities using synchrotron X-ray can be sufficiently large to measure the relatively small fractions of carbide present in each of the specimens.
  Experiments were conducted on The Swedish Materials Science Beamline P21.2 at PETRA III in the Deutsches Elektronen-Synchrotron. The X-ray wavelength was 0.2066 Å, monochromated using diffraction. X-ray detection was done using a PILATUS3 X CdTe 2M detector with pixel size of 172 μm × 172 μm. The sample detector distance was determined to be 2800 mm to allow the largest possible diffraction at $2\theta<15°$, where the most intense peaks of carbides are expected. The X-ray beam size was chosen to be 0.5 mm × 0.5 mm with a dwell time of 5 s per measurement point. Hundreds of images were captured, spaced out evenly across each specimen. Analysis was performed using Python modules; pyFAI-calib2 for detector calibration and pyFAI-integrate for data reduction. Rietveld analysis using *MAUD*[30] was used to calculate the volume fraction of carbides.
- Energy dispersive X-ray analysis in a transmission electron microscope was used to identify the carbides and measure their compositions.

III. RESULTS AND DISCUSSION

A. *Carbides Precipitated Before Hydrogen Exposure*

The results of synchrotron X-ray analysis are presented in Figure 2.

Figure 3 compares the Baker and Nutting findings on the types of carbide observed, with the data determined using synchrotron X-ray analysis for the specific steel used here. Although there is broad agreement, only Sample A completely complies with the original work. It is speculated that discrepancies for other specimens might be because of the detailed difference in the heat treatment, for example the cooling rate during quenching or air cooling, which is affected by the size of the specimen. Nevertheless, the purpose of using different heat treatments was to precipitate a variety of combinations of carbides and that was achieved.

Phase stability calculations using *ThermoCalc* (TCFE10 database)[31] were used to estimate equilibrium carbide volume fractions and their chemical compositions. It is appreciated that these represent

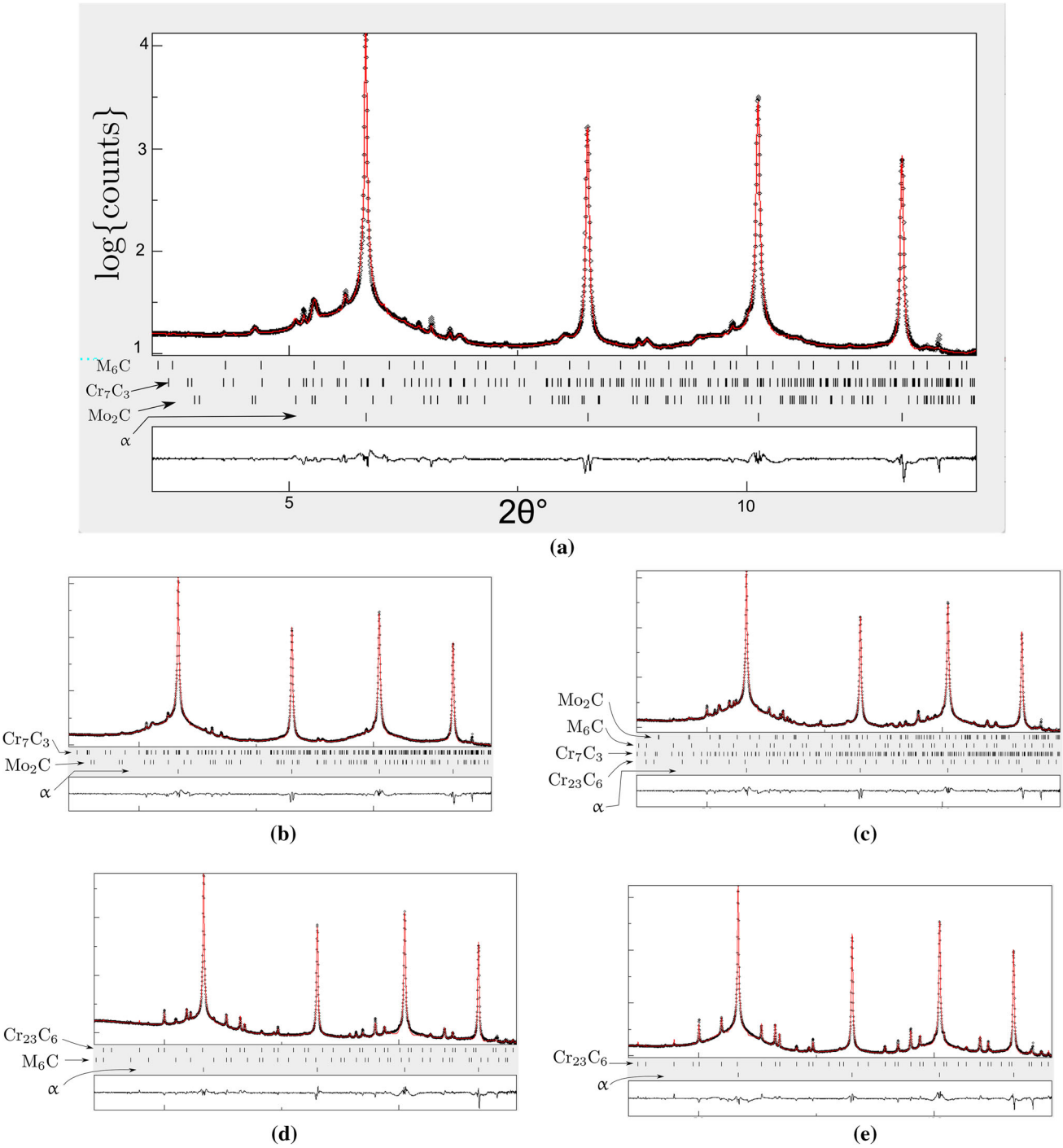

Fig. 2—Synchrotron X-ray line profiles. (*a*) Sample A. Note that the scales for all the remaining profiles are identical to those of sample A. (*b*) Sample B. (*c*) Sample C. (*d*) Sample D. (*e*) Sample E.

thermodynamic equilibrium rather than kinetics, but as will be seen later, they nevertheless can give useful information in interpreting complex observations. Figure 4 shows that for all the tempering temperatures investigated in the present work, the only carbide to be able to exist in equilibrium with ferrite is $M_{23}C_6$. All other carbides that are observed in the steel therefore must be regarded as transient. It still is useful to characterise the equilibrium for these transient carbides. This was done in the calculations by suppressing the most stable carbide in the precipitation sequence to allow the transients to appear; these calculations are henceforth referred to as constrained equilibria.

Table III compares the carbide volume fractions expected by *ThermoCalc* and those measured using synchrotron X-rays before hydrogen exposure. The comparison shows that with the heat treatments implemented, most of the carbides did not reach the expected

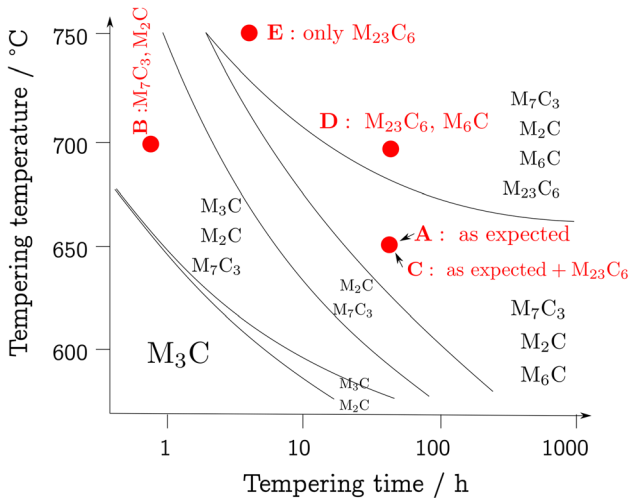

Fig. 3—Carbides as expected from Nutting[28] and as found here. In red are the current findings with samples represented by their designated letters (Table V) (Color figure online).

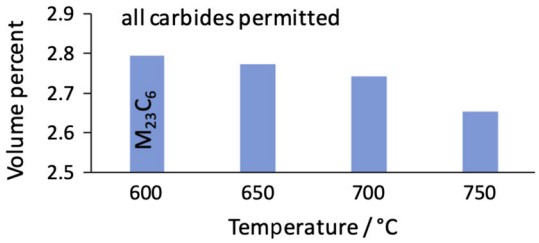

Fig. 4—Equilibrium calculations for the alloy listed in Table I. M_3C, M_6C, $M_{23}C_6$, M_2C, M_7C_3, where 'M' represents the metal atoms Fe, Cr, Mo, were all allowed to exist in the calculations, together with the residual phase α. No carbide other than $M_{23}C_6$ was predicted at equilibrium.

equilibrium nor constrained-equilibrium volume fractions. The exceptions being samples D and E in which the $M_{23}C_6$ and M_6C both are approximately at equilibrium. This is because those samples were tempered at the highest temperatures. Table IV shows the equilibrium composition of carbides at the tempering temperatures used in this work.

As emphasised earlier, only the equilibrium $M_{23}C_6$ values were obtained while allowing all the other carbides to exist in the calculations. The same applies to the data for Sample D, where the volume fraction of M_6C is very small and the agreement between the thermodynamically calculated and actual fraction of $M_{23}C_6$ is consequently good. On the other hand, M_7C_3 and M_6C values could only be estimated after *suppressing* $M_{23}C_6$. M_2C and cementite values were obtained similarly after suppressing $M_{23}C_6$ and M_7C_3.

Therefore, the comparison between the *equilibrium* thermodynamic estimates and measured data are strictly only valid for Sample E which contained just $M_{23}C_6$; the agreement there is excellent. The rest of the calculations represent constrained equilibria, which if given sufficient time at temperatures would eventually reach equilibrium, but have not done so with the heat treatments

Table III. Volume Fractions of Carbides as Expected Under Equilibrium or Constrained-Equilibrium Conditions Using *ThermoCalc* (Calculated) and as Determined Using Synchrotron X-ray Diffraction (Measured) for the Heat-Treated Specimens

	Sample A, Quench → 650°C, 50 h		Sample B, Quench → 700°C, 1 h		Sample C, air cool → 650°C, 50 h		Sample D, air cool → 700°C, 50 h		Sample E, air cool → 750°C, 5 h	
	Calculated	Measured	Calculated	Measured	Calculated	Measured	Calculated	Measured	Calculated	Measured
M_6C	0.0037	0.0022 ± 0.0003	—	—	0.0037	0.0031 ± 0.0005	0.0008	0.0004 ± 0.0002	—	—
M_2C	0.0131	0.0026 ± 0.0001	0.0067	0.0039 ± 0.0001	0.0131	0.0010 ± 0.0001	—	—	—	—
M_7C_3	0.0154	0.0087 ± 0.0006	0.0172	0.0071 ± 0.0006	0.0152	0.0048 ± 0.0007	—	—	0.0263 ± 0.0008	0.0263 ± 0.0008
$M_{23}C_6$					0.0276	0.0113 ± 0.0008	0.02718	0.0271 ± 0.0008	0.02636	0.0263 ± 0.0008

Table IV. *ThermoCalc* Prediction of Equilibrium Chemical Composition (Weight Pct) for Carbides as a Function of Temperature for $2\frac{1}{4}$Cr-1Mo Steel

	M_3C			M_2C			M_6C		
	650 °C	700 °C	750 °C	650 °C	700 °C	750 °C	650 °C	700 °C	750 °C
C	6.86	6.83	6.81	6.56	6.79	0.02	2.52	2.56	2.59
Cr	40.70	35.52	30.97	11.57	15.09	2.74	2.93	3.44	3.76
Mo	1.04	1.22	1.44	79.70	74.51	0.79	66.69	64.17	61.69
Fe	48.38	54.01	58.94	1.83	3.36	94.68	27.38	29.32	31.45
Mn	2.98	2.36	1.78	0.32	0.23	0.89	0.00	0.00	0.00

	M_7C_3			$M_{23}C_6$		
	650 °C	700 °C	750 °C	650 °C	700 °C	750 °C
C	8.41	8.41	8.40	5.05	5.07	5.10
Cr	54.32	50.90	47.17	37.87	34.31	30.69
Mo	10.50	9.80	9.38	18.44	16.94	14.69
Fe	24.33	28.79	33.32	38.14	43.12	48.91
Mn	2.41	2.07	1.68	0.33	0.38	0.43

The composition of $M_{23}C_6$ is when all carbides were permitted to exist but only $M_{23}C_6$ was predicted in association with α. Those of M_7C_3 and M_6C are for the case where $M_{23}C_6$ was suppressed. The compositions of M_2C and cementite represent the case where M_2C, cementite and M_6C were only allowed to exist.

Table V. Void or Inclusion Volume Fractions Before and After Hydrogen Exposure

Unexposed Sample	Inclusion Volume Fraction $8 \times 10^{-5} \pm 9 \times 10^{-6}$
Sample	Void + inclusion volume fraction
A (Quenched, → 650 °C for 50 h)	$47 \times 10^{-5} \pm 2 \times 10^{-5}$
B (Quenched, → 700 °C for 1 h)	$46 \times 10^{-5} \pm 2 \times 10^{-5}$
C (Air cooled, → 650 °C for 50 h)	$120 \times 10^{-5} \pm 3 \times 10^{-5}$
D (Air cooled, → 700 °C for 50 h)	$52 \times 10^{-5} \pm 2 \times 10^{-5}$
E (Air cooled, → 750 °C for 5 h)	$33 \times 10^{-5} \pm 3 \times 10^{-5}$

The quantities for the exposed specimens include the inclusion fraction from the unexposed state. The error bars were calculated by dividing the standard deviation by the square root of the number of measurements.

implemented. In contrast, Samples A-C show metastable microstructures so closure is not expected with the equilibrium calculations.

B. *Void Fractions After Hydrogen Exposure*

In the initial state, the steel contains only non-metallic inclusions but no voids. The inclusion fraction was measured prior to hydrogen exposure, using microscopy imaging of unetched specimens then analysed using *ImageJ* software, as $V_V = 8 \times 10^{-5} \pm 9 \times 10^{-6}$. The same method was used to characterise the *increase* in the void volume fraction following hydrogen attack. The increase was then identified as voids introduced during hydrogen exposure. A summary of the results is listed in Table V. Sample C has the highest V_V, which suggests that it underwent the highest hydrogen attack rate with an increase of two orders of magnitude after hydrogen exposure. This was followed by sample D, A + B in terms of descending V_V, with the least damage in sample E. Samples A, B, D and E had an increase in V_V by one order of magnitude in comparison to the state prior to exposure.

The increase in void volume fraction following hydrogen exposure (Table V) might correlate with the reduction of carbide volume fractions. To investigate how the carbides resisted hydrogen attack, synchrotron X-ray analysis was carried out on the hydrogen-exposed specimens to permit the accurate measurement of small volume fractions.

C. *Carbide Fractions Following Hydrogen Exposure*

A representation of how the synchrotron X-ray analysis was carried out on the specimens is shown in Figure 5. Measurements were conducted horizontally from surface to surface. After the whole sample has been examined, all values from the same position were averaged to give one spectrum for that location, which was then analysed using Rietveld analysis to estimate carbide fractions at that position. The first and last

positions are also the nearest with respect to the hydrogen-exposed surface.

According to the data in Table V, Samples A and B were the 2nd least damaged specimens in terms of the reduction in carbide volume fractions. Synchrotron X-ray analysis showed no noticeable reduction in carbides except for one position for M_7C_3 in sample B. M_2C and M_6C showed good resistance to reaction with hydrogen as their fractions remained stable, explaining the good overall-resistance of those two specimens.

Sample C exhibited the least resistance to hydrogen attack. The void volume fraction increased by two orders of magnitude relative to the unexposed specimen, Table V. Figure 6 shows that the reduction was greatest for $M_{23}C_6$ in sample C with its volume fraction reduced from 0.0113 ± 0.0008 in the unexposed specimen to as low as 0.0051 ± 0.0005 in one of the positions in the exposed specimen, a reduction of 0.0062. Figure 6 shows that M_7C_3 also decreased from 0.0048 ± 0.0007 in the unexposed specimen to 0.0021 ±0.0006 at one of the positions in the exposed specimen. M_2C and M_6C fractions remained essentially unchanged.

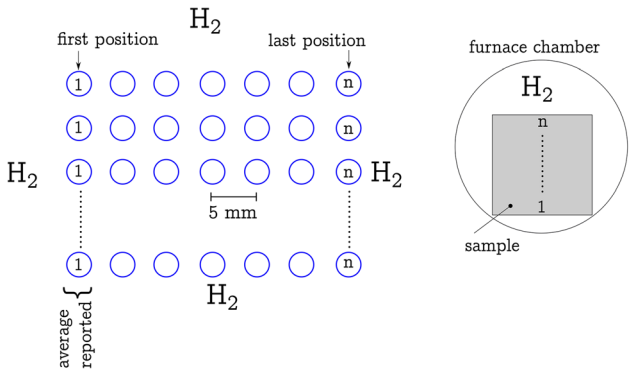

Fig. 5—A representation of how measurements are taken with synchrotron X-ray for hydrogen-exposed specimens. The sketch on the right shows how the square-sectioned sample was placed within the autoclave during hydrogen exposure. As a result, position 1 has less access to hydrogen than position *n*.

M_6C also resisted attack in sample D. The increase in V_V in this specimen is caused by the reduction of $M_{23}C_6$, which was reduced by 0.0056, a similar reduction to that observed in sample C., as seen in Figure 7. This specimen was ranked 2nd in terms of susceptibility to hydrogen attack.

The smallest increase in V_V was observed in sample E, which contained only $M_{23}C_6$. The high tempering temperature (750 °C) influences the composition of $M_{23}C_6$ making it closer to its equilibrium composition, Table VI, which will be discussed later. This explains the excellent hydrogen attack resistance in this specimen.

It is interesting to note that a greater degree of carbide-depletion is observed towards one of the specimen surfaces in Figures 6 and 7. The specimen positioning, Figure 5, suggests that the access to constant high hydrogen pressures is less to the bottom of the specimen than other areas, which could introduce a difference in carbide-depletion amounts. Those heavily depleted regions correspond to the top end of the specimens in Figure 5, where access to hydrogen pressure is continuously greater.

The voids volume fraction can be seen to correspond to the depletion of carbides by Figure 8 that shows the gradient of voids area percentage across specimen C.

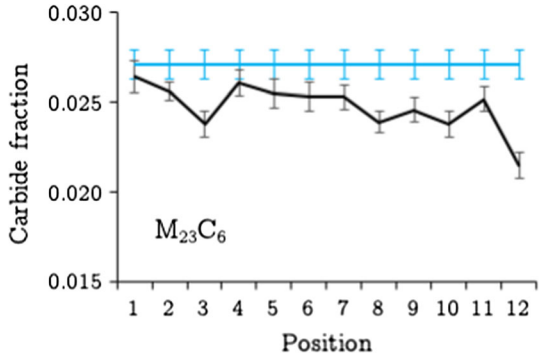

Fig. 7—Sample D. The fraction prior to exposure is represented by the blue line. First and last positions represent the closest proximity to the exposed surface (Color figure online).

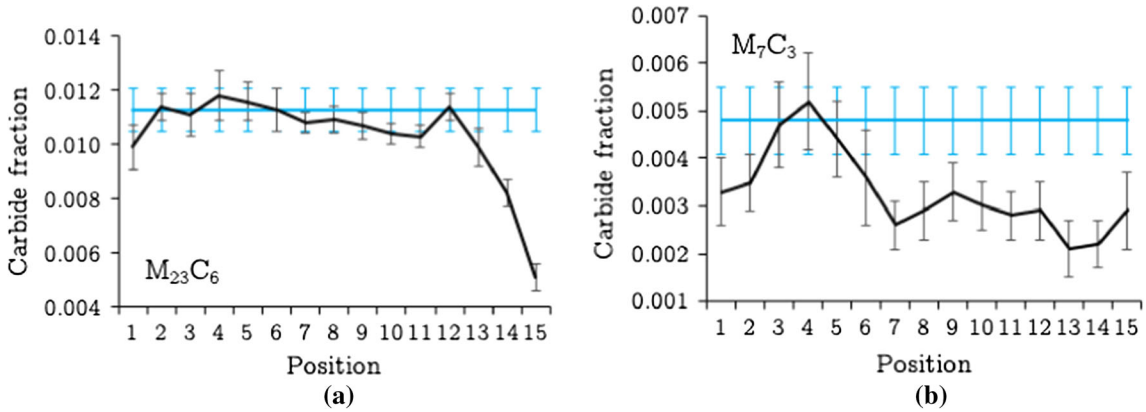

Fig. 6—Sample C. The fractions prior to exposure are represented by the blue lines. First and last positions represent the closest proximity to the exposed surface. M_2C and M_6C fractions remained essentially unchanged, so are not plotted here (Color figure online).

Table VI. Equilibrium and Measured Chemical Composition (Weight Pct) of $M_{23}C_6$ at Different Tempering Temperatures

	Sample C, air cool → 650°C, 50 h		Sample D, air cool → 700°C, 50 h		Sample E, air cool → 750°C, 5 h	
	Calculated	EDX	Calculated	EDX	Calculated	EDX
C	5.052		5.071		5.107	
Cr	37.877	15.61 ± 0.20	34.317	16.01 ± 0.13	30.691	27.43 ± 0.05
Mo	18.448	6.62 ± 0.13	16.943	3.93 ± 0.07	14.692	4.90 ± 0.03
Fe	38.146	70.04 ± 0.42	43.129	71.79 ± 0.26	48.916	58.33 ± 0.07
Mn	0.332	2.68 ± 0.10	0.385	3.19 ± 0.05	0.435	4.23 ± 0.02

Carbon content used was calculated by *ThermoCalc* and EDX measurements for other elements were corrected accordingly.

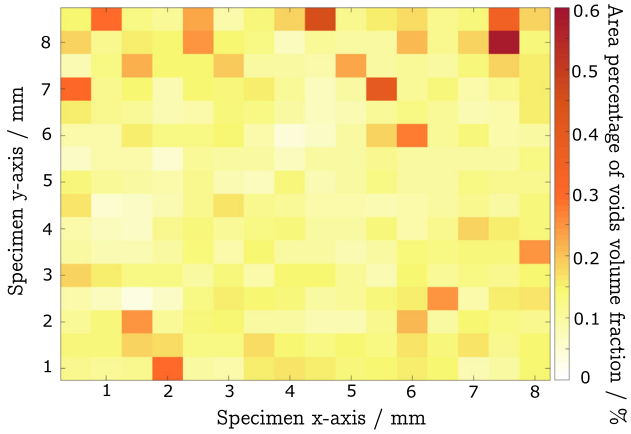

Fig. 8—A representation of the cross section of specimen C that underwent the highest attack. Each square represents a micrograph that was analysed by ImageJ. Higher voids formation in the vicinity of the edges is assumed to correlate to the hydrogen ingress into the specimen. Voids have formed more towards the top of the specimen due to the greater access to hydrogen pressure because of the positioning showed in Fig. 5.

Each square represents a micrograph that was analysed by ImageJ to calculate the voids volume fraction. Note that the top of Figure 8 corresponds to the top of specimen when it was positioned in the autoclave as shown in Figure 5. It can be seen from Figure 8 that more voids have formed in the vicinity of the edges of the specimen, where exposure to hydrogen is expected to be the highest. It can also be seen that voids have formed at the top part of the specimen more than its bottom, where access to hydrogen pressure is continuously greater due to specimen positioning showed in Figure 5. The gradient of voids being the most towards the edges of the specimen shows the correlation between the voids formation and hydrogen ingress into the steel.

In summary, Mo-rich carbides, M_2C and M_6C, seem to resist attack under all the conditions studied more than Cr-rich carbides, where resistance was more dependent on the extent of tempering. M_7C_3 and $M_{23}C_6$ resistance varied between samples. Therefore, hydrogen attack resistance cannot be decided on the basis of the carbide type alone. It may depend on other factors such as heat treatment, i.e., quenched or normalised, and tempering temperature and duration. M_7C_3 in $2\frac{1}{4}$Cr-1Mo steel are transient carbides (Figure 4) and to eventually be replaced by $M_{23}C_6$, which explains why its fraction decreases. In order to investigate Cr-carbides further, the behaviour of $M_{23}C_6$ was examined as it showed low resistance in samples C and D, but high resistance in sample E.

D. *Effect of Deviation from Equilibrium*

$M_{23}C_6$ showed poor hydrogen attack resistance in samples C and D as it depleted by about 0.006 of its original volume fractions, while the hydrogen attack resistance of $M_{23}C_6$ was excellent in sample E. Samples C and D were tempered for 50 h at 650 °C and 700 °C, respectively, while sample E was tempered at 750 °C for 5 h. Therefore, the hydrogen attack resistance of $M_{23}C_6$ increased as the tempering temperature increased. In terms of equilibrium, calculations showed that $M_{23}C_6$ should be the only carbide present at equilibrium at all tempering temperatures (Figure 4). Not surprisingly, this suggests that only sample E was at equilibrium as it contained only $M_{23}C_6$.

For further investigation, the chemical composition of $M_{23}C_6$ was calculated at equilibrium using *ThermoCalc* and measured experimentally using energy dispersive X-ray analysis in a transmission electron microscope. The results are listed in Table VI; the chromium concentration within $M_{23}C_6$ is clearly much less than equilibrium for samples C and D. Parathasarathy and Shewmon investigated the correlation between hydrogen attack rates and carbon activity against the atom fraction of chromium in the matrix ferrite,[32] in which they concluded that a high chromium content in the matrix indicates a low iron content, hence a reduced carbon activity, which must lead to a greater hydrogen attack resistance, Figure 9. The calculations are based on the estimation of the carbon activity that is in equilibrium with $M_{23}C_6$ using the reaction

$$y_{Cr}Cr + \frac{6}{23}C + y_{Fe}Fe = (Fe_{y_{Fe}}Cr_{y_{Cr}})C_{6/23}$$

where $y_{Fe} = x_{Fe}/(x_{Fe} + x_{Cr})$, with x representing the mole fraction of the solute identified in the subscript. It follows that $y_{Cr} = 1 - y_{Fe}$. The standard-free energy change for this reaction was compiled from thermodynamic data[33,34] as

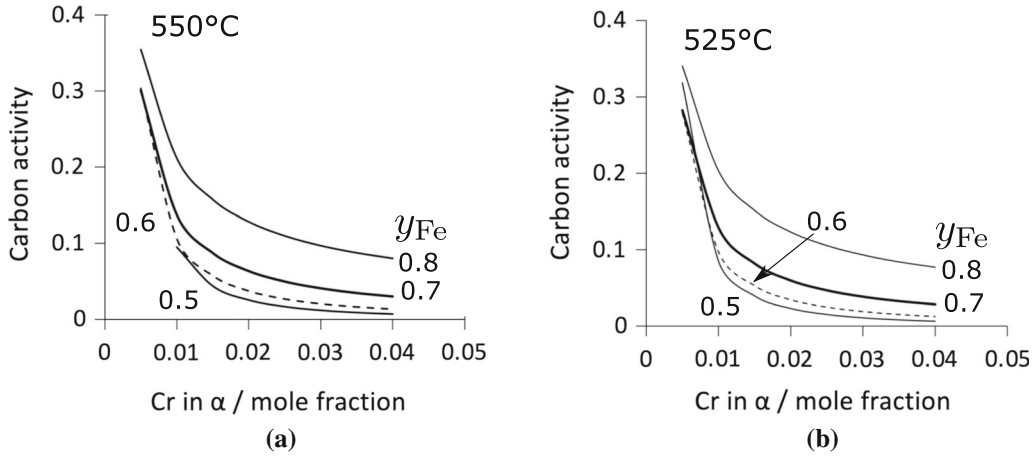

Fig. 9—Calculations using Equation 2. (*a*) The relationship of carbon activity with the atom fraction chromium in the matrix for various atom fractions of iron in the carbide metal content in $2\frac{1}{4}$Cr-1Mo steel for the temperature used by Parthasarathy and Shewmon.[32] Adapted from Ref. [32] by permission from Springer Nature. (*b*) Calculations for the temperature representative of the present experiments.

$$\begin{aligned}\Delta G^\circ =& y_{Cr}\left(G^\circ_{CrC_{6/23}} + G^\circ_{Cr} - \frac{6}{23}G^\circ_C\right)\\ &+ y_{Fe}\left(G^\circ_{FeC_{6/23}} + G^\circ_{\alpha Fe} - \frac{6}{23}G^\circ_C\right)\\ &+ RT(y_{Fe}\ln\{y_{Fe}\} + y_{Cr}\ln\{y_{Cr}\})\\ &+ y_{Fe}y_{Cr}1100 \qquad \text{J mol}^{-1}\end{aligned}$$

so that the equilibrium constant K in terms of the activities a_i is given by

$$K = \exp\left\{-\frac{\Delta G^\circ}{RT}\right\} = \frac{a_{MC_{6/23}}}{a_{Cr}^{y_{Cr}} \times a_{Fe}^{y_{Fe}} \times a_C^{6/23}}.$$

Using this, Parathsarathy and Shewmon went on to isolate the activity of carbon as

$$a_C = \exp\left\{\frac{\Delta G^\circ}{RT}\right\}\frac{a_{MC_{6/23}}}{(a_{Cr}^{y_{Cr}} \times a_{Fe}^{y_{Fe}})^{23/6}} \qquad [1]$$

but the equation is incorrect; it should in fact be

$$a_C = \left[\exp\left\{\frac{\Delta G^\circ}{RT}\right\}\frac{a_{MC_{6/23}}}{a_{Cr}^{y_{Cr}} \times a_{Fe}^{y_{Fe}}}\right]^{23/6}. \qquad [2]$$

It has been verified that the original error was typographical, their results are correct as indicated by our calculations in Figure 9(a) which compares well with Figure 5 of Reference 32, showing how the activity of carbon in the matrix varies with the matrix concentration of chromium and the ratio y_{Fe}/y_{Cr}. Since the temperature they used for their calculations differed slightly from our experiments, Figure 9(b) shows the results of relevant behaviour for 525 °C, using Equation [2].

The data in Table VI show that the Fe and Cr concentrations are not close to equilibrium when tempering at 650 °C to 700 °C, because the measured Cr concentrations should be much larger, making the $M_{23}C_6$ more reactive at the lower temperatures. This explains the difference in hydrogen attack behaviour of $M_{23}C_6$ when generated using different tempering temperatures. Therefore, if equilibrium conditions for $M_{23}C_6$ are reached for low tempering temperatures (650 °C), the carbon activity would be minimised, thereby decreasing the tendency to react with hydrogen and form methane. But unfortunately, the tempering times required would be impractical as literature has shown that not even 500 h at 700 °C would ensure equilibrium conditions,[32] unless the temperature is increased as seen in sample E (750 °C).

It is interesting to mention that equilibrium Cr concentrations decrease with increasing tempering temperature, as seen in Table VI, suggesting that greater concentrations of Cr dissolved in ferrite that is tempered at a higher temperature.

Table VI also shows that the molybdenum concentration in $M_{23}C_6$ is much smaller than consistent with equilibrium, for all the samples listed. However, this measured concentration of molybdenum is similar for all the samples listed, so probably does not play are role in differentiating the hydrogen attack behaviour of the three samples.

E. *Effect of Microstructure*

Samples A and C were both tempered at 650 °C for 50 h. Sample A was quenched to martensite before tempering while sample C was air cooled into a bainitic state before tempering. Sample C has greater hydrogen attack damage than sample A (Table V). This difference cannot be attributed to the tempering treatment, but possibly to microstructure prior to tempering. Of course, sample E also had a bainitic initial microstructure but it was tempered much more severely to almost reach equilibrium, so its excellent attack resistance is clearly a consequence of the high chromium concentration in its sole carbide, $M_{23}C_6$.

The carbides expected in both specimens C, D are M_7C_3, M_6C and M_2C, but also $M_{23}C_6$ in sample D (Figure 3). However, synchrotron X-ray indicated that

$M_{23}C_6$ was precipitated in sample C along with the expected carbides, while sample A contained only the transition carbides.

To understand why alloy carbide precipitation is slower in the initially martensitic microstructure, it is important to understand that the bainite- and martensite-start temperatures of the steel are 547 and 421 °C, respectively, so the bainite forms at a temperature where there is significantly greater atomic mobility. Tsai and Yang[35] conducted detailed electron microscopy for a sample of $2\frac{1}{4}$Cr-1Mo steel tempered at 700 °C to show that alloy carbides form more rapidly when the initial state is bainitic. This might be expected from the higher transformation temperature, the microstructure in effect being partly tempered during transformation. Furthermore, the martensite is expected to contain a greater density of dislocations; the formation of cementite during the early stages of tempering would therefore be retarded because carbon is more stable at dislocations than in cementite.[36] Given that the volume fractions of the transient alloy carbides as measured in sample A are almost identical to the corresponding carbides in sample C, it must be concluded that sample A has not completed the precipitation process and this applies also to sample B.

If the total amount of carbon that is in the form of carbides ($w_{carbide}$), is calculated, then using the experimentally measured data from Table III and assuming stoichiometry,

	$w_{carbide}$ / wt *pct*	$w_{residue}$ / wt *pct*	a_{before} / Å	a_{after} / Å
Sample A	0.106 ± 0.007	0.038 ± 0.007	2.868	2.869
Sample B	0.098 ± 0.007	0.042 ± 0.007	2.869	2.869
Sample C	0.121 ± 0.013	0.019 ± 0.013	2.868	2.868
Sample D	0.146 ± 0.012	0.0	2.868	2.868
Sample E	0.140 ± 0.011	0.0	2.868	2.868

where $w_{residue}$ represents the difference between the average carbon concentration (0.14 wt pct) and that tied up in carbides. The residual concentrations might seem large given the high-temperature tempering experienced by all of these samples. However, in a 0.17C-9.3Cr-1.6Mo-0.27V wt pct steel cooled to martensite and then tempered at 590 °C for 8 h and then at 700 °C for 16 h, atom probe measurements revealed the tempered ferrite to contain 0.035 wt pct of carbon within the ferrite matrix that results from the tempering of martensite.[37] After creep at 600 °C for 14522 h at 160 MPa, the carbon concentration in the ferrite decreased to 0.0151 wt pct,[38] which still is much greater than consistent with the equilibrium of alloy carbides with ferrite.

It is likely that any excess carbon is located at defects rather than in solid solution; the lattice parameters do not show significant variation between the samples in both the initial (a_{before}) and exposed (a_{after}) exposed states; the error bars in the measurements of lattice parameters are less than ± 0.001 Å.

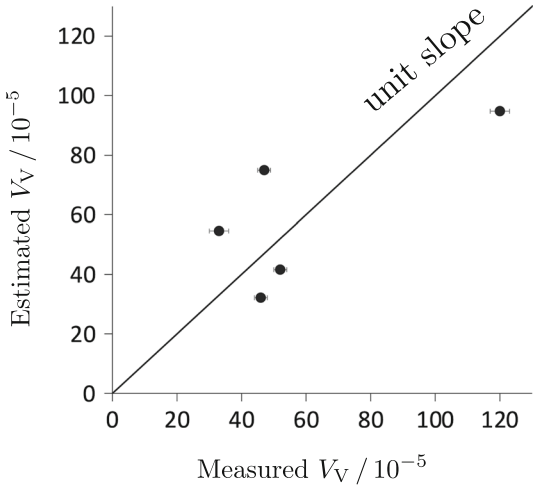

Fig. 10—The estimated void fraction against that measured, using only the residual carbon concentration and the measured volume fraction of $M_{23}C_6$.

If the carbon is located at defects such as dislocations, then the martensite should contain more excess carbon than bainite, because of its greater dislocation density, explaining the larger residual concentration in samples A and B.

It is clear from the samples studied that both the residual carbon concentration in the ferrite, and the fraction of $M_{23}C_6$ precipitation play a role. The multiple regression analysis illustrated in Figure 10 shows that these two variables can explain a large amount of the observed variation in the tendency to form voids, albeit with a correlation coefficient of only 0.74. If V_V^{total} and V_V^{void} represent the inclusion + void and void volume fractions, respectively, then the corresponding regression equations are:

$$\frac{V_V^{total}}{10^{-5}} = 481 - 16266 V_V^{M_{23}C_6} - 10695 w_{residue} \quad \pm 33$$

and $$V_V^{void} = V_V^{total} - 8 \times 10^{-5}$$

where $w_{residue}$ is in weight percent and the relationships applicable over the ranges studied here.

Probably, the most important missing variable is the chromium content of the $M_{23}C_6$, which clearly will influence the activity of the carbon in the matrix, Figure 9. Since this carbide did not form in samples A and B, there are only three data points available for samples C-E in Table VI. Since multiple regression with three variables and three data is not possible, the V_V^{total} was regressed against the chromium concentration of $M_{23}C_6$,

$$\frac{V_V^{total}}{10^{-5}} \approx -4.7 w_{wt\ pct\ Cr}^{M_{23}C_6} + 161 \qquad [3]$$

with a correlation coefficient of 0.7. The negative coefficient is consistent with a greater chromium concentration reducing the activity of carbon in the ferrite.

IV. CONCLUSIONS

Some really quite interesting and unexpected data have been obtained on the tendency for hydrogen attack, expressed as the fraction of voids generated, have emerged from the examination of a classical $2\frac{1}{4}$Cr-1Mo steel subjected to a variety of heat treatments prior to exposure.

- The heat treatment influenced the hydrogen attack resistance. It was shown that the same steel grade could be susceptible to or resist hydrogen attack at the same exposure conditions, which was successfully correlated to the heat treatment. This suggests that design against hydrogen attack-based solely on temperature, hydrogen pressure and steel grade, as done in the Nelson curves, could fall short, as was seen in Tesoro refinery.[19]
  It was possible to quantitatively measure the hydrogen damage by utilizing a new experimental matrix that includes microscopy techniques combined with synchrotron X-ray diffraction. The experimental results helped in gaining new insights about the mechanism such as the importance of the equilibrium state of carbides, which is influenced by heat treatments. Specifying heat treatment requirements could be a vital addition to the design standard.
- The carbon activity is not just a function of carbide-type but also of tempering conditions that are important in determining the tendency for hydrogen attack. The tempering conditions influence the equilibrium state of the carbides, hence carbon activity and hydrogen attack susceptibility. For example, only the heat treatment at 750 °C for 5 h led to consistency between the thermodynamically calculated equilibrium chromium concentration and that measured within $M_{23}C_6$. Since the activity of carbon in the ferrite depends on the Cr/Fe ratio within the carbide, a less than expected Cr concentration within $M_{23}C_6$ leads to a greater degree of hydrogen attack and this is why $M_{23}C_6$ underwent hydrogen attack when equilibrium state was not reached.
- The elevated temperature tempering rate of an initially martensitic state is slower than that of a bainitic microstructure when considering the sequence of substitutionally alloyed carbides. This is probably a consequence of the greater defect density of martensite, which means that more carbon is retained at defects. It is well-known, for example, that carbon located at defects has a greater stability than in cementite, although similar studies have not been done for alloyed carbides.
- The concentrations of carbon left in the ferrite, even after the severe tempering treatments implemented here, can be far in excess of the concentration in equilibrium with $M_{23}C_6$. The excess has the effect of retarding the attack of hydrogen on carbides, because the ferrite must first be decarburised by the hydrogen.
  This somewhat contradicts a theoretical conclusion by Schlögl *et al.* where it is argued that the it is important to have as little carbon as possible in the ferrite, based on a calculation of methane pressure within a void.[39] But we note that only the concentration of carbon in ferrite that is in *equilibrium* with the carbide was considered and that those values are much smaller than recorded here, because equilibrium thermodynamics does not consider the defect structures.

ACKNOWLEDGMENTS

This work was funded by the Oil & Gas Network Integrity Division in the Research & Development Centre, Saudi Aramco. We acknowledge DESY (Hamburg, Germany), a member of the Helmholtz Association HGF, for the provision of experimental facilities. Parts of this research were carried out at PETRA III and we would like to thank Dr. Magnus Hörnqvist Colliander for assistance in using Beamline P21.2. Beamtime was allocated for proposal I-20190135 EC.

CONFLICT OF INTEREST

The authors declare that they have no conflict of interest.

REFERENCES

1. H.K.D.H. Bhadeshia: *ISIJ Int.*, 2016, vol. 56, pp. 24–36.
2. X. Li, X. Ma, J. Zhang, E. Akiyama, Y. Wang, and X. Song: *Acta Metall. Sin.*, 2020, vol. 33, pp. 759–73.
3. S. Hall: *Rules of thumb for chemical engineers*. Elsevier, 5th edition edition, 2012.
4. M. W. D. Van Der Burg, E. Van Der Giessen, and R. C. Brouwer: *Acta Metall.*, 1996, vol. 44, pp. 505–18.
5. S.S. Vagarali, and G.R. Odette: *Metall. Trans. A*, 1981, vol. 12, pp. 2071–82.
6. T. A. Parthasarathy: *Acta Metall.*, 1985, vol. 33, pp. 1673–81.
7. H.C. Furtado, and I.L. May: *Mater. Res.*, 2004, vol. 7, pp. 103–10.
8. D.J. Benac, and P. McAndrew: *J. Fail. Anal. Prevent.*, 2012, vol. 12, pp. 624–27.
9. T.A. Parthasarathy, H.F. Lopez, and P.G. Shewmon: *Metall. Trans. A*, 1985, vol. 16A, pp. 1143–49.

10. J.R. Thygeson, and M.C. Molstad: *J. Chem. Eng. Data*, 1964, vol. 9, pp. 309–15.
11. P.G. Shewmon: *Metall. Trans. A*, 1976, vol. 7A, pp. 279–86.
12. D. Eliezer: *J. Mater. Sci.*, 1981, vol. 16, pp. 2962–66.
13. T.G. Kim: *Eng. Fail. Anal.*, 2002, vol. 9, pp. 571–78.
14. M.L. Martin, M. Dafarnia, S. Orwig, D. Moore, and P. Sofronis: *Acta Mater.*, 2017, vol. 140, pp. 300–04.
15. S.Z. Chavoshi, L.T. Hill, K.E. Bagnoli, R.L. Holloman, and K.M. Nikbin: *Eng. Fail. Anal.*, 2020, vol. 117, 1.
16. K. Poorhaydari: *J. Mater. Eng. Perform.*, 2021, vol. 30, pp. 7875–7980.
17. F.K. Naumann: *Stahl Eisen*, 1937, vol. 57, pp. 889–99.
18. F.K. Naumann: *Stahl Eisen*, 1938, vol. 58, pp. 1239–50.
19. Anonymous. Catastrophic rupture of heat exchanger (seven fatalities). Technical Report https://www.csb.gov/tesoro-refinery-fatal-explosion-and-fire/, U. S. Chemical Safety and Hazard Investigation Board, Washington, DC, USA (2014).
20. G.R. Prescott, and B. Shannon: *Ammonia Plant Saf. Relat. Facilities*, 2001, vol. 41, pp. 237–53.
21. G.A. Nelson: *Am. Petrol. Inst. Proc.*, 1949, vol. 29, pp. 163–72.
22. Anonymous. The technical basis document for API RP 941. Technical Report API TR 941-A, American Petroleum Institute, Washington, DC, USA (2019).
23. E.E. Fletcher, and A.R. Elsea: *The effects of high-pressure, high-temperature hydrogen on steel* (Technical report, Battelle Memorial Institute, 1964).
24. J. Hucinska: *Adv. Mater. Sci.*, 2003, vol. 4, pp. 21–27.
25. M.W.D. Van Der Burg, E. Van der Giessen, and V. Tvergaard: *Mater. Sci. Eng.*, 1998, vol. A241, pp. 1–13.
26. S.M. Schlogl, Y. van Leeuwen, and E. van der Giessen: *Metall. Mater. Trans. A*, 2000, vol. 31A, pp. 125–37.
27. R.G. Baker, and J. Nutting: *J. Iron Steel Inst.*, 1959, vol. 192, pp. 257–68.
28. J. Nutting: The structural stability of low alloy steels for power generation applications, in *Advanced Heat Resistant Steels for Power Generation*. ed. by R. Viswanathan, J. Nutting. pp. (Institute of Materials, London, UK, 1998), pp. 12–30.
29. J. Wanagel, T. Hakkarainen, and C. Y. Li: *Steel Thick-Wall Pressure*, pp. 93–108, Ohio, USA (1982). ASM International.
30. L. Lutterotti: Materials analysis using diffraction, http://www.ing.unitn.it/~maud/index.html. Last accessed 27 Feb (2013).
31. B. Sundman, B. Jansson, and J.O. Andersson: *CALPHAD*, 1985, vol. 9, pp. 153–90.
32. T.A. Parthasarathy, and P.G. Shewmon: *Metall. Trans. A*, 1984, vol. 15, pp. 2021–27.
33. R. Lundberg, M. Waldenstrom, and B. Uhrenius: *CALPHAD*, 1977, vol. 1, pp. 159–99.
34. L. Kaufman, E.V. Clougherty, and R.J. Weiss: *Acta Metall.*, 1963, vol. 11, pp. 323–35.
35. M.C. Tsai, and J.R. Yang: *J. Mater. Sci.*, 2003, vol. 38, pp. 2373–91.
36. D. Kalish, M. Cohen, and S.A. Kulin: *J. Mater.*, 1970, vol. 5, pp. 169–83.
37. P. Hofer, M.K. Miller, S.S. Babu, S.A. David, and H. Cerjak: *Metall. Mater. Trans. A*, 2000, vol. 31B, pp. 975–84.
38. P. Hofer, M.K. Miller, S.S. Babu, S.A. David, and H. Cerjak: *ISIJ Int.*, 2002, vol. 42, pp. 562–66.
39. S. M. Schlogl, J. Svoboda, and E. van der Giessen: *Acta Mater.*, 2001, vol. 49, pp. 2227–38.